J. Fluid Mech. (2012), *vol.* 690, *pp.* 321–344. © Cambridge University Press 2011
doi:10.1017/jfm.2011.432

Boundary-layer-separation-driven vortex shedding beneath internal solitary waves of depression

Payam Aghsaee[1], Leon Boegman[1]†, Peter J. Diamessis[2] and Kevin G. Lamb[3]

[1] Environmental Fluid Dynamics Laboratory, Department of Civil Engineering, Queen's University, Kingston, Ontario, K7L 3N6, Canada

[2] School of Civil and Environmental Engineering, Cornell University, Ithaca, New York, USA

[3] Department of Applied Mathematics, University of Waterloo, Ontario, N2L 3G1, Canada

(Received 10 November 2010; revised 7 September 2011; accepted 29 September 2011; first published online 24 November 2011)

We investigate global instability and vortex shedding in the separated laminar boundary layer beneath internal solitary waves (ISWs) of depression in a two-layer stratified fluid by performing high-resolution two-dimensional direct numerical simulations. The simulations were conducted with waves propagating over a flat bottom and shoaling over relatively mild ($S = 0.05$) and steep ($S = 0.1$) slopes. Over a flat bottom, the potential for vortex shedding is shown to be directly dependent on wave amplitude, for a particular stratification, owing to increase of the adverse pressure gradient ($\mathrm{d}P/\mathrm{d}x > 0$ for leftward propagating waves) beneath the trailing edge of larger amplitude waves. The generated eddies can ascend from the bottom boundary to as high as 33 % of the total depth in two-dimensional simulations. Over sloping boundaries, global instability occurs beneath all waves as they steepen. For the slopes considered, vortex shedding begins before wave breaking and the vortices, shed from the bottom boundary, can reach the pycnocline, modifying the wave breaking mechanism. Combining the results over flat and sloping boundaries, a unified criterion for vortex shedding in arbitrary two-layer continuous stratifications is proposed, which depends on the momentum-thickness Reynolds number and the non-dimensionalized ISW-induced pressure gradient at the point of separation. The criterion is generalized to a form that may be readily computed from field data and compared to published laboratory experiments and field observations. During vortex shedding events, the bed shear stress, vertical velocity and near-bed Reynolds stress were elevated, in agreement with laboratory observations during re-suspension events, indicating that boundary layer instability is an important mechanism leading to sediment re-suspension.

Key words: boundary layer stability, internal waves, ocean processes

1. Introduction

Internal solitary waves (ISWs) are ubiquitous in stratified lakes and oceans (e.g. Helfrich & Melville 2006; Jackson 2007; Shroyer, Moum & Nash 2009). Localized

† Email address for correspondence: leon.boegman@civil.queensu.ca

https://doi.org/10.1017/jfm.2011.432 Published online by Cambridge University Press

occurrence of bed sediment re-suspension has been attributed to their passage in the field (e.g. Bogucki, Dickey & Redekopp 1997; Klymak & Moum 2003; Butman *et al.* 2006; Quaresma *et al.* 2007; Reeder, Ma & Yang 2011) and in the laboratory (e.g. Boegman & Ivey 2009). Re-suspension is believed to occur due to the instability of the separated ISW-induced bottom boundary layer in the adverse-pressure-gradient region beneath the wave (e.g. Bogucki & Redekopp 1999; Bogucki, Redekopp & Barth 2005; Carr & Davies 2006; Stastna & Lamb 2008).

The instability is global, as opposed to local, in that there is a streamwise dependence in the base-state velocity profile (Huerre 2000). The streamwise variability results from the presence of a separation bubble (region of re-circulating fluid), confined between points of boundary layer separation and reattachment. The length scale of streamwise variation of the base-state velocity profile associated with the separation bubble is long compared to the wavelength of the resulting global instability (Huerre 2000). This instability is spontaneously excited, i.e. it does not require any external noise. For a sufficiently strong adverse pressure gradient, the vorticity in the ISW-induced boundary layer is rolled up into coherent vortices that are quasi-periodically shed into the water column (Diamessis & Redekopp 2006; Stastna & Lamb 2008). Over sloping topography, the vortices interact with the pycnocline of the shoaling wave modifying the breaking mechanism (e.g. Sveen *et al.* 2002; Aghsaee, Boegman & Lamb 2010).

There has been considerable effort applied to developing a predictive criterion for global instability and associated re-suspension in geophysical flows. Global instability beneath ISWs of elevation, over a flat bottom and in the presence of a background shear flow, is dependent upon the background flow characteristics, wave amplitude and Reynolds number (Bogucki & Redekopp 1999; Stastna & Lamb 2002, 2008). Diamessis & Redekopp (2006), for their particular stratification profile, proposed a stability boundary, for both ISWs of elevation and depression without a background current, that was a function of wave amplitude (a/H) and ISW Reynolds number ($Re_w = c_0 H/\nu$), where H is the total water column depth, c_0 is the linear wave phase speed and ν is the kinematic viscosity. However, their proposed stability boundary is inconsistent with recent laboratory findings (Carr, Davies & Shivaram 2008); c_0 depends only on the stratification and H is a general length scale that has no knowledge of the wave amplitude and wave length. On the other hand the momentum-thickness Reynolds number at the separation point ($Re_{\theta_{sep}} = U\theta_{sep}/\nu$) has been used as an appropriate parameter in studying boundary layer instability in aerodynamics (e.g. Gaster 1969; Pauley, Moin & Reynolds 1990). Here

$$\theta_{sep} = \int_0^{z(U)} u/U(1 - u/U)\,\mathrm{d}z \tag{1.1}$$

is momentum thickness and $u(z)$ and U are horizontal velocity and inviscid horizontal velocity (as if there were a free-slip bottom boundary, thus no separation; Gaster 1969) at the separation point. Moreover, the stability boundary proposed by Diamessis & Redekopp (2006) cannot be generalized to different stratification profiles because different waves, with equal a/H but different wavelengths (and perhaps different pressure gradients), can have the same Re_w (Stastna & Lamb 2008). The above-mentioned studies investigate global instability associated with laminar boundary layers where the adverse pressure gradient beneath ISWs will always lead to flow separation (e.g. Carr & Davies 2006). The existence of a turbulent bottom boundary layer, as is commonly observed in lakes and oceans (e.g. Lemckert *et al.* 2004;

https://doi.org/10.1017/jfm.2011.432 Published online by Cambridge University Press

Nimmo Smith, Katz & Osborn 2005) will add more complexity to the problem and is not addressed here. Turbulent boundary layers are more resistant than laminar ones to flow separation in an adverse-pressure-gradient region and require stronger pressure gradients for flow separation to occur (e.g. Wang, Bogucki & Redekopp 2001).

The ability of transient vortices, associated with shoaling ISWs of depression, to re-suspend bed material has been studied in the lab and correlated to the wave-coherent vortex-induced Reynolds stress above the viscous sub-layer. The vortex applies a sediment mobilizing shear stress and sediment re-suspending vertical velocity (Boegman & Ivey 2009). Re-suspension associated with solitary waves of elevation, with trapped cores, has also been observed in the field, where it is associated with the vortex inside the trapped core (Hosegood & van Haren 2004; Bonnin *et al.* 2006).

The objective of the present study is to investigate the laminar boundary layer instability mechanism beneath ISWs of depression over both flat and sloping topography. Both types of topographies are considered because the adverse pressure gradient will respond to changes in stratification and wave amplitude over a flat bottom and to changes in lower-layer thickness over sloping topography. We seek to formulate a criterion for predicting the occurrence of global instability and investigate the potential for the unstable flow to re-suspend bed material. Background theory is given in § 2, followed by a description of the two-dimensional (2D) numerical model used in this study in § 3. In § 4 we present our results and introduce a threshold for vortex shedding based on the gradual evolution of the separation bubble. We introduce a shedding criterion and discuss the possibility of bed-sediment re-suspension associated with the boundary layer instability in § 5. Summary and conclusions are presented in § 6.

2. Theoretical background

The generation and propagation of weakly nonlinear dispersive ISWs is theoretically described by the Korteweg–de Vries (KdV) equation

$$\eta_t + c_0\eta_x + \alpha\eta\eta_x + \beta\eta_{xxx} = 0, \tag{2.1}$$

where $\eta(x, t)$ is the vertical displacement of the pycnocline (e.g. Apel 2002). For a two-layer stratified fluid, with a thin pycnocline relative to the total depth, the nonlinearity and dispersion coefficients (α and β, respectively) and the linear wave phase speed (c_0) are

$$\alpha = \frac{3c_0}{2}\frac{h_1 - h_2}{h_1 h_2}, \quad \beta = \frac{c_0}{6}h_1 h_2, \tag{2.2}$$

$$c_0 = \sqrt{\frac{g' h_1 h_2}{h_1 + h_2}} \tag{2.3}$$

(e.g. Djordjevic & Redekopp 1978). Here h_1 and h_2 are the upper layer (fluid with density ρ_1) and lower layer (fluid with density ρ_2) thicknesses, respectively, and $g' = g(\rho_2 - \rho_1)/\rho_2$ is the reduced gravity under the Boussinesq approximation. A two-layer stratification is typically observed in lakes where $h_1 < h_2$. In the ocean, the stratification is more complex; however, a surface mixed layer overlying a deeper stratified lower layer is often observed (e.g. Moum *et al.* 2003; Warn-Varnas *et al.* 2007; Shroyer *et al.* 2009) and modelled as a two-layer stratification (e.g. Liu *et al.* 1998). Most of the observed ISWs in the ocean are waves of depression (negative wave amplitude a; figure 1), which for a two-layer fluid occurs when $h_1 < h_2$. Several

https://doi.org/10.1017/jfm.2011.432 Published online by Cambridge University Press

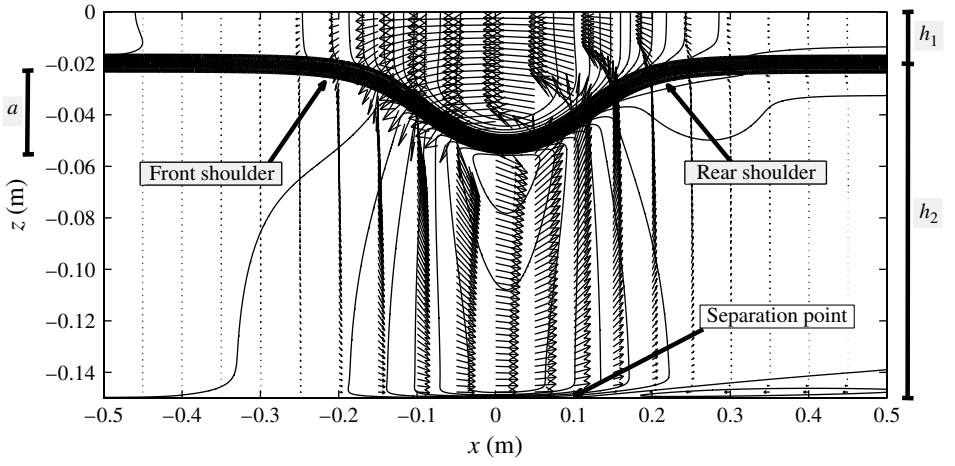


FIGURE 1. Instantaneous velocity field (vectors) associated with an ISW of depression (a is positive upward) travelling from right to left (simulation 6F). Thick and thin lines represent density and horizontal velocity contours respectively. Deceleration and subsequent flow separation are evident beneath the rear face of the wave.

observations of waves of elevation have also been made on the shelf (e.g. Klymak & Moum 2003; Orr & Mignerey 2003). The characteristic horizontal length scale associated with a KdV wave is $\lambda = \sqrt{12\beta/\alpha a}$, which decreases with increasing $|a|$ for a given stratification. However, by retaining only the first-order nonlinear terms, the KdV equation is only valid for ISWs where $|a| << (h_2 - h_1)/2$ (Lamb & Wan 1998). As $|a|$ becomes larger, the displaced interface gets close to the mid-depth (i.e. $|a| \to (h_2 - h_1)/2$), and solutions of the fully nonlinear equations under the Boussinesq approximation show that waves broaden horizontally (e.g. Lamb & Wan 1998; Helfrich & Melville 2006), generating broad-crested ISWs that deviate significantly from the sech^2 KdV wave profile. This limits the maximum possible wave amplitude $|a|_{max} \to (h_2 - h_1)/2$. To consider both broad-crested and KdV waves, in this study, we apply a more general horizontal wavelength scale (e.g. Koop & Butler 1981; Michallet & Ivey 1999)

$$L_w = \frac{1}{a}\int_{-\infty}^{+\infty} \eta(x)\,\mathrm{d}x, \tag{2.4}$$

where $a = \eta_{min}(x)$. Flow visualization suggests that the observed wavelength $L \sim 2L_w$ for narrow-crested ISWs where $|a| < (h_2 - h_1)/2$ (Aghsaee *et al.* 2010). L_w is important in determining the boundary layer thickness $\delta \sim \sqrt{\nu L_w/c}$ beneath the ISW trough (Helfrich & Melville 1986) where c is the ISW propagation speed.

The velocity field associated with a typical ISW of depression travelling from right to left (figure 1) shows that the horizontal wave-induced velocity varies from its maximum value beneath the wave trough to zero behind the wave. Hence there is always a decelerating adverse-pressure-gradient region underneath the rear half of the wave. The pressure gradient is difficult to measure observationally, and is modelled to balance advection using the steady inviscid momentum equation in a reference frame moving with the wave

$$-\frac{1}{\rho}\frac{\mathrm{d}P}{\mathrm{d}x} = (U + c)\frac{\mathrm{d}U}{\mathrm{d}x}, \tag{2.5}$$

https://doi.org/10.1017/jfm.2011.432 Published online by Cambridge University Press

which is valid at the edge of the boundary layer, where U and P are the free-stream horizontal velocity and pressure. For a given stratification, a larger amplitude wave (more nonlinear) has both a greater wave-induced lower -layer velocity beneath its trough

$$U_2 = \frac{-ca}{h_2 - a} \tag{2.6}$$

(Ostrovsky & Stepanyants 2005) and a steeper wave front (Aghsaee *et al.* 2010), and as a result will exhibit stronger flow separation.

Flow separation always occurs in laminar boundary layers under ISWs of depression (Wang *et al.* 2001; Carr & Davies 2006), where the distribution of free-stream velocity $U(x)$ is concave downward behind its maximum ($\mathrm{d}^2U/\mathrm{d}x^2 < 0$; Schlichting 1979). However, turbulent boundary layers are capable of stabilizing much stronger pressure gradients than laminar ones (Schlichting 1979), and for a particular stratification the ISW amplitude should exceed a critical value for separation to occur in an ISW-driven bottom boundary layer that is already turbulent (Wang *et al.* 2001).

3. Methods: numerical model and simulation parameters

A two-dimensional nonlinear non-hydrostatic computational fluid dynamics model (Lamb & Nguyen 2009) was applied to numerically simulate ISWs at laboratory scale. The model solves the incompressible Navier–Stokes equations, using a σ-layer coordinate system, for a Newtonian fluid with the Boussinesq approximation:

$$\frac{\partial u}{\partial t} + u\frac{\partial u}{\partial x} + w\frac{\partial u}{\partial z} = -\frac{1}{\rho_0}\frac{\partial p}{\partial x} + \nu\nabla^2 u, \tag{3.1}$$

$$\frac{\partial w}{\partial t} + u\frac{\partial w}{\partial x} + w\frac{\partial w}{\partial z} = -\frac{1}{\rho_0}\frac{\partial p}{\partial z} - \frac{\rho g}{\rho_0} + \nu\nabla^2 w, \tag{3.2}$$

$$\frac{\partial \rho}{\partial t} + u\frac{\partial \rho}{\partial x} + w\frac{\partial \rho}{\partial z} = k\nabla^2 \rho, \tag{3.3}$$

$$\frac{\partial u}{\partial x} + \frac{\partial w}{\partial z} = 0, \tag{3.4}$$

where (x, z) are the horizontal and vertical coordinates and (u, w) are the associated velocity vectors, P and ρ are pressure and density, respectively, $\rho_0 = (\rho_1 + \rho_2)/2$ is a reference density, and k is the molecular diffusivity. A no-slip boundary condition was applied along the bottom and two end walls and a free-slip condition was applied at the surface rigid lid (Lamb & Nguyen 2009). A no-flux boundary condition was used for the density field on all boundaries. A tanh density profile

$$\bar{\rho}(z) = \frac{\rho_1 + \rho_2}{2} - \frac{\rho_2 - \rho_1}{2}\tanh\left(\frac{z - z_{pyc}}{d_{pyc}}\right) \tag{3.5}$$

approximates a laboratory generated two-layer stratified fluid (e.g. Boegman & Ivey 2009). Here, z varies between 0 at the surface and $-H$ at the bottom and z_{pyc} and d_{pyc} determine the location and half-thickness of the pycnocline, respectively.

The model is initialized with an ISW obtained by solving the Dubreil–Jacotin–Long (DJL) equation, expressed in terms of streamline displacement (Lamb 2002, his equation 6). The total depth of the domain, $H = 0.15$ m, matches conditions from previous laboratory experiments (Michallet & Ivey 1999) with $\rho_1 = 1000$ kg m^{-3} and $\rho_2 = 1040$ kg m^{-3}. Over the flat bottom, each wave travels from right to left

https://doi.org/10.1017/jfm.2011.432 Published online by Cambridge University Press

No.	d_{pyc} (m)	h_1 (m)	a (m)	$\frac{a+h_1}{H}$	L_w (m)	$\frac{x_{sep}}{L_w}$	w_{max}/c_0	$Re_{\theta_{sep}}$	$P_{x_{sep}}$	$\frac{a}{H}$	Re_w ($\times 10^5$)	VS
1F	0.0040	0.010	−0.042	0.35	0.20	0.40	0.006	98.5	0.095	0.28	3.63	N
2F	0.0040	0.010	−0.047	0.38	0.21	0.39	0.010	94.8	0.122	0.31	1.81	N
3F	0.0040	0.010	−0.047	0.38	0.22	0.38	0.090	130.1	0.123	0.31	3.63	Y
4F	0.0065	0.010	−0.053	0.42	0.26	0.33	0.420	179.9	0.168	0.36	3.63	Y
5F	0.0065	0.010	−0.057	0.45	0.29	0.31	0.490	161.3	0.184	0.38	1.81	Y
6F	0.0025	0.020	−0.032	0.35	0.25	0.39	0.005	14.0	0.059	0.21	0.12	N
7F	0.0025	0.020	−0.032	0.38	0.25	0.35	0.005	62.8	0.065	0.21	2.47	N
8F	0.0065	0.020	−0.052	0.48	0.47	0.30	0.410	212.2	0.132	0.35	2.47	Y
9F	0.0080	0.020	−0.053	0.49	0.54	0.31	0.480	248.5	0.127	0.35	2.47	Y
10F	0.0100	0.020	−0.053	0.49	0.59	0.24	0.008	60.7	0.114	0.36	0.12	N
11F	0.0100	0.020	−0.053	0.49	0.59	0.31	0.540	192.0	0.122	0.36	1.23	Y
12F	0.0100	0.020	−0.053	0.49	0.59	0.32	0.700	267.2	0.127	0.36	2.47	Y
13F	0.0100	0.020	−0.053	0.49	0.59	0.34	0.700	335.6	0.138	0.36	4.93	Y
14F	0.0100	0.030	−0.040	0.47	0.50	0.30	0.100	178.0	0.092	0.27	2.90	Y
15F	0.0100	0.030	−0.044	0.49	0.85	0.32	0.006	205.6	0.069	0.29	1.45	N
16F	0.0100	0.030	−0.044	0.49	0.85	0.34	0.260	290.6	0.073	0.29	2.90	Y
17F	0.0100	0.030	−0.044	0.49	0.85	0.35	0.430	384.4	0.079	0.29	5.80	Y
18F	0.0100	0.035	−0.039	0.49	0.70	0.31	0.010	213.6	0.066	0.26	3.06	N
19F	0.0100	0.041	−0.041	0.50	1.06	0.34	0.009	233.8	0.052	0.27	1.91	N
20F	0.0100	0.035	−0.039	0.49	1.06	0.35	0.190	297.7	0.054	0.26	3.06	Y
21F	0.0100	0.040	−0.036	0.50	1.34	0.34	0.007	281.1	0.037	0.24	3.20	N
22F	0.0100	0.040	−0.036	0.50	1.80	0.38	0.001	378.6	0.030	0.24	3.20	N

TABLE 1. Experimental parameters for the numerical simulations over a flat bottom. Subscript *sep* denotes values computed at the separation point and VS indicates the occurrence of vortex shedding. The horizontal coordinate x is zero at the wave trough (figure 1). $P_{x_{sep}}$ is the pressure gradient non-dimensionalized by $\rho_0 g'$; $Re_{\theta_{sep}}$ is the momentum-thickness Reynolds number at the separation point. The total depth is $H = 0.15$ m for all simulations.

in a frame of reference moving with the wave phase speed. For each stratification the wave amplitude was increased up to $a \approx (h_2 - h_1)/2$, at which point the ISW trough starts broadening and the pressure gradient does not change significantly. The Reynolds number was increased by decreasing the viscosity. By positioning 8–10 vertical grids within the separated boundary layer, we resolve the bottom boundary layer. The horizontal grid spacing was 1.25 times that in the vertical direction. Results were grid-independent at these resolutions. The Prandtl number (Pr) was set to 1. Table 1 summarizes the main simulation parameters.

Simulations of four different ISWs shoaling over two different slopes with $S = 0.05$ and 0.1 were undertaken. The waves travel from left to right. Viscosities of $\nu = 10^{-6}, 2 \times 10^{-7}$ and 5×10^{-8} m^2 s^{-1} were used and Pr was set to 1. The σ-coordinate system increased the grid resolution as the waves travelled up the sloping boundary. For the most viscous simulations ($\nu = 10^{-6}$ m^2 s^{-1}), 150 σ-layers were used and the horizontal spacing was 2.5 times the vertical spacing away from the slope. For $\nu = 2 \times 10^{-7}$ m^2 s^{-1} and 5×10^{-8} m^2 s^{-1} four times the number of grid points were used in each direction. The results were grid-independent at these resolutions. The simulation parameters associated with these simulations are presented in table 2.

https://doi.org/10.1017/jfm.2011.432 Published online by Cambridge University Press

https://doi.org/10.1017/jfm.2011.432 Published online by Cambridge University Press

			$S = 0.1$					$S = 0.05$				
$h_1(m)$	d_{pyc} (m)	a (m)	No.	$Re_{\theta_{sep}}$	$P_{x_{sep}}$	w_{max}/c_0	BKE/ISWE (%)	No.	$Re_{\theta_{sep}}$	$P_{x_{sep}}$	w_{max}/c_0	BKE/ISWE (%)
							$\nu = 5 \times 10^{-8}$ m^2 s^{-1}					
0.05	0.0015	0.013	1A	297.2	0.082	0.82	3.73	**5A**	230.8	0.064	0.86	5.49
0.04	0.0015	0.016	2A	248.1	0.093	1.12	5.26	**6A**	207.2	0.069	0.90	6.59
0.02	0.0015	0.013	3A	156.7	0.100	1.09	5.80	**7A**	141.4	0.074	0.90	7.08
0.02	0.0025	0.032	4A	230.6	0.115	1.81	4.39	**8A**	203.3	0.080	1.46	4.30
							$\nu = 2 \times 10^{-7}$ m^2 s^{-1}					
0.05	0.0015	0.013	1B	146.7	0.094	0.70	4.28	**5B**	120.3	0.063	0.70	6.90
0.04	0.0015	0.016	2B	124.1	0.100	0.82	6.24	**6B**	106.1	0.069	0.85	8.21
0.02	0.0015	0.013	3B	80.3	0.100	1.04	6.62	**7B**	70.5	0.071	0.92	9.67
0.02	0.0025	0.032	4B	115.1	0.115	1.73	5.43	**8B**	101.8	0.076	1.35	6.69
							$\nu = 10^{-6}$ m^2 s^{-1}					
0.05	0.0015	0.013	1C	41.5	0.106	0.54	7.02	**5C**	50.1	0.073	0.38	9.98
0.04	0.0015	0.016	2C	58.2	0.108	0.54	8.52	**6C**	53.1	0.068	0.39	9.64
0.02	0.0015	0.013	3C	36.4	0.112	0.57	9.89	**7C**	30.7	0.075	0.39	14.82
0.02	0.0025	0.032	4C	49.8	0.117	0.97	7.41	**8C**	49.0	0.083	0.66	10.69

TABLE 2. Experimental parameters for the numerical simulations over sloping bottom boundaries. Subscript *sep* denotes parameters computed at the separation point. $P_{x_{sep}}$ is the pressure gradient non-dimensionalized by $\rho_0 g'$ and $Re_{\theta_{sep}}$ is the momentum-thickness Reynolds number at the separation point. The maximum vertical velocity (w_{max}), kinetic energy within the separation bubble and shed vortices (BKE), and total energy of the wave (ISWE) (Lamb & Nguyen 2009, equations 10 and 14 therein respectively) were calculated when the first vortices were shed. Here, c_0 is the linear phase speed of the offshore wave and the total depth is $H = 0.15$ m for all simulations.

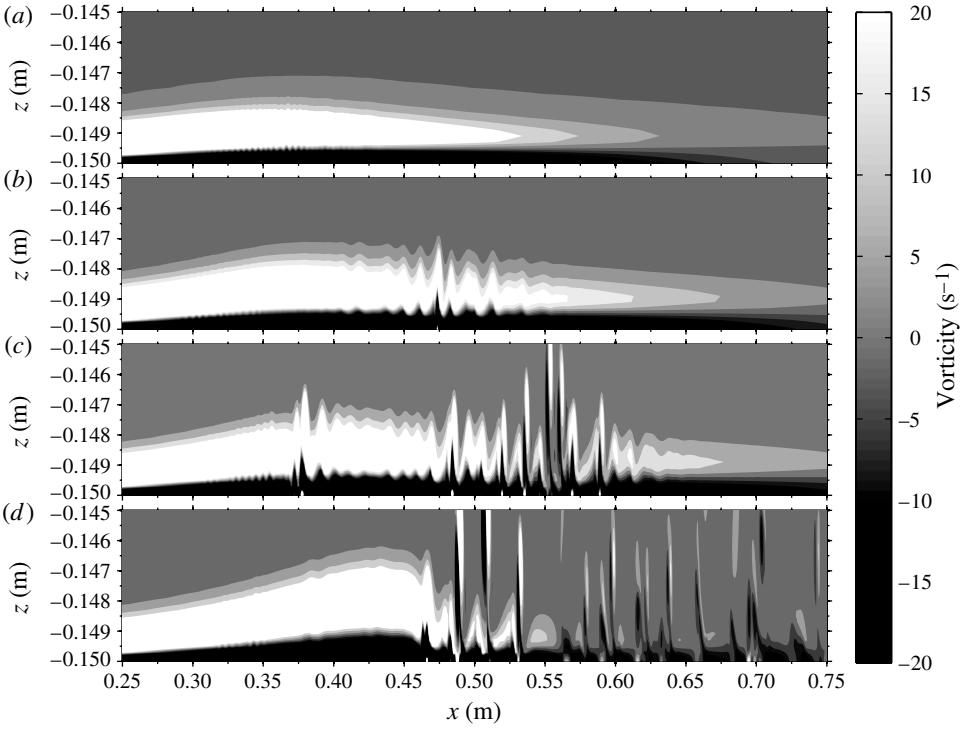


FIGURE 2. Evolution of separation bubble instability and subsequent vortex shedding (simulation 12F). Shaded contours show the vorticity field forming two parallel vortex sheets that eventually turn into shed vortices, distorting the separation bubble and lifting off the bed; (*a–d*) correspond to non-dimensional time $t^* = tc_0/H = 1.86$, 2.51, 2.95 and 4.59 respectively, where t is time. The wave is propagating leftward.

4. Results

4.1. *Separation bubble dynamics over a flat bottom*

Flow separation occurs as the wave travels over a no-slip boundary, forming a reverse flow (jet) in the deceleration region beneath the rear face of the wave (e.g. figure 1; Diamessis & Redekopp 2006; Carr *et al.* 2008). The separation point (where $\mathrm{d}u/\mathrm{d}z = 0$) is located between $0.24L_w$ and $0.4L_w$ from the wave trough toward the wave rear face (table 1).

The time evolution of the separated flow and the occurrence of global instability, beneath the wave, can be observed in the vorticity field (figure 2); here the wave is travelling from right to left (figure 3, corresponding to the same time instant as figure 2*d*). Figure 2(*a*) shows the separation bubble to be composed of two contiguous parallel vortex sheets with opposite sign, where the lower sheet represents the boundary layer associated with the reverse flow and the upper one is due to the separated flow overlying it. As time evolves, both vortex sheets grow vertically and spread horizontally in the direction opposite to that of wave propagation (figure 2*b*). For a stable boundary layer, they grow gradually until they achieve steady state. During growth, they can also become globally unstable, leading to vortex shedding, where eddy structures lift from the vortex sheets (figures 2*c* and 2*d*) distort their shape and travel in the direction of wave propagation, while progressing slower than the wave phase speed (Carr *et al.* 2008). Shedding occurs intermittently, alternating with

https://doi.org/10.1017/jfm.2011.432 Published online by Cambridge University Press

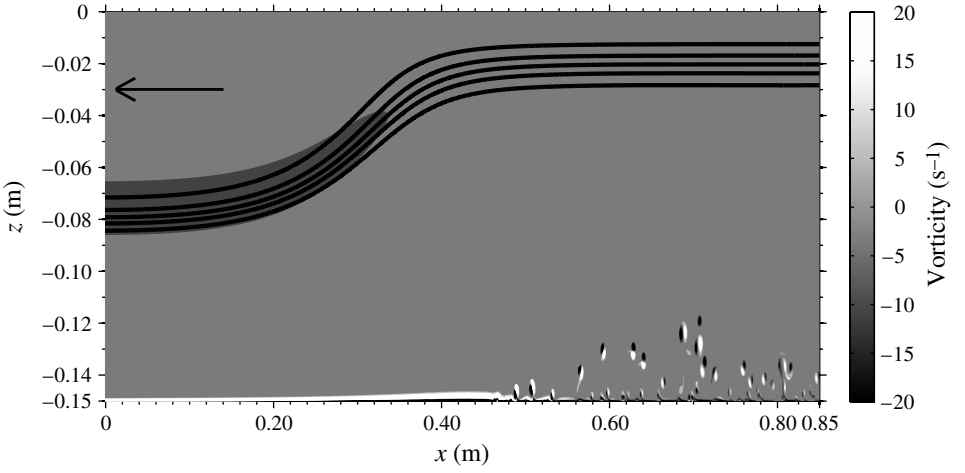


FIGURE 3. Expanded view of vorticity field corresponding to figure 2(*d*). Thick lines show density contours with density jump of 5 kg m^{-3} across each contour. The shed vortices beneath the rear face have lifted to 27 % of the total depth at this particular time.

calm periods (Stefanakis 2010), during which the bubble temporarily reconstructs itself until the next set of vortex ejections begins (figure 2*d*).

The vortices are much smaller than the ISW (figure 3), the difference in scale increasing with Reynolds number (Aghsaee *et al.* 2010), and are observed to rise into the water column from the bed (e.g. Diamessis & Redekopp 2006). In a three-dimensional flow, the eddies may degenerate more rapidly than in these two-dimensional simulations due to secondary three-dimensional lateral instabilities as well as transition to turbulence at sufficiently high Reynolds numbers that cannot be modelled in our two-dimensional simulations (Jones, Sandberg & Sandham 2008). Therefore, the focus of this study is on the initial evolution of the instabilities where the wave-induced bottom boundary layer remains two-dimensional in the absence of any external three-dimensional perturbations. The secondary characteristics of the flow will be the subject of future work.

Two main parameters contribute to the stability characteristics of the separation bubble; first, the strength of the flow separation, which is measured with the adverse pressure gradient ($\mathrm{d}P/\mathrm{d}x > 0$) and second, a Reynolds number associated with separation ($Re_{\theta_{sep}}$). For each stratification these parameters will be largest for broad-crested waves, which have the maximum possible wave amplitude for a given stratification (see § 1), leading to the maximum possible lower-layer velocity U_2 (2.6). Vortex shedding is more likely for these types of waves than for narrow-crested waves, consistent with our results (table 1; 7F versus 8F).

4.2. *Separation bubble dynamics over sloping boundaries*

For an ISW shoaling over a sloping bottom boundary, the associated flow field, boundary layer and adverse pressure gradient characteristics change continuously as the wave shoals. When the wave trough approaches the bottom boundary, the horizontal velocity beneath the wave increases and the rear face of the wave steepens, increasing both the magnitude of the horizontal velocity gradient and, according to (2.5), the adverse pressure gradient.

https://doi.org/10.1017/jfm.2011.432 Published online by Cambridge University Press

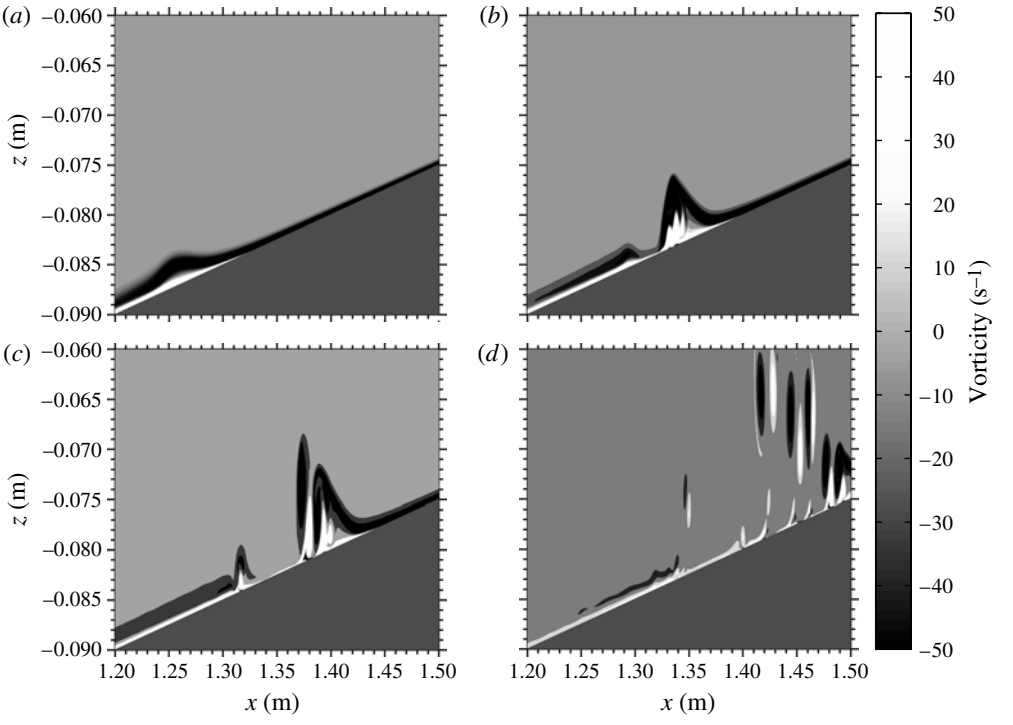


FIGURE 4. Same as figure 2, but for simulation 8A with $S = 0.05$; (*a–d*) refer to $t^* = tc_0/H = 10.06$, 10.66, 11.06 and 11.87 respectively. The wave is propagating to the right.

Eventually the adverse pressure gradient becomes sufficiently strong that vortex shedding occurs (e.g. figure 4). This process is characterized by the two parallel vortex sheets bending toward the vertical and detaching from the bottom boundary (figures 4*a* and 4*b*). Eddies shed from the bottom boundary (figures 4*c* and 4*d*), are similar to the flat bottom simulations. A distinguishing characteristic of the separation bubble instability over a sloping bottom boundary, relative to a flat bottom, is the distortion (vertical bending and stretching) of the separation bubble. This is probably due to the fact that the pycnocline is much closer to the bottom, in which the adverse pressure gradient continuously increases as the wave shoals. The eddies play an important role in regulating the ISW breaking mechanism (Sveen *et al.* 2002; Aghsaee *et al.* 2010) as they can eventually reach the pycnocline and lead to its instability (i.e. ISW breaking; figure 5 corresponding to the same time instant as figure 4*d*).

The importance of vortex shedding to ISW dynamics over sloping and flat bottoms, can be quantified by the ratio of the kinetic energy in the separation bubble and eddies (calculated by integrating the kinetic energy density over the eddy area) to the total ISW energy (calculated by integrating kinetic energy and available potential energy densities over the total domain). As an ISW shoals, the energy transfer from the ISW to the separated flow increases from ∼1–10 % at the initiation of instability (e.g. figure 4*b*) to ∼4–15 % at the time of first shedding (e.g. figure 4*c*) (table 2). This leads to the average energy transfer rate of 2–6 % s^{-1}. Over mild slopes, wave breaking by plunging is delayed, resulting in energy flux to the eddies until they have sufficient strength to influence the breaking mechanism, causing collapsing breaking to occur (Aghsaee *et al.* 2010). Over flat bottoms, $<\sim 1$ % of the ISW energy is transferred

https://doi.org/10.1017/jfm.2011.432 Published online by Cambridge University Press

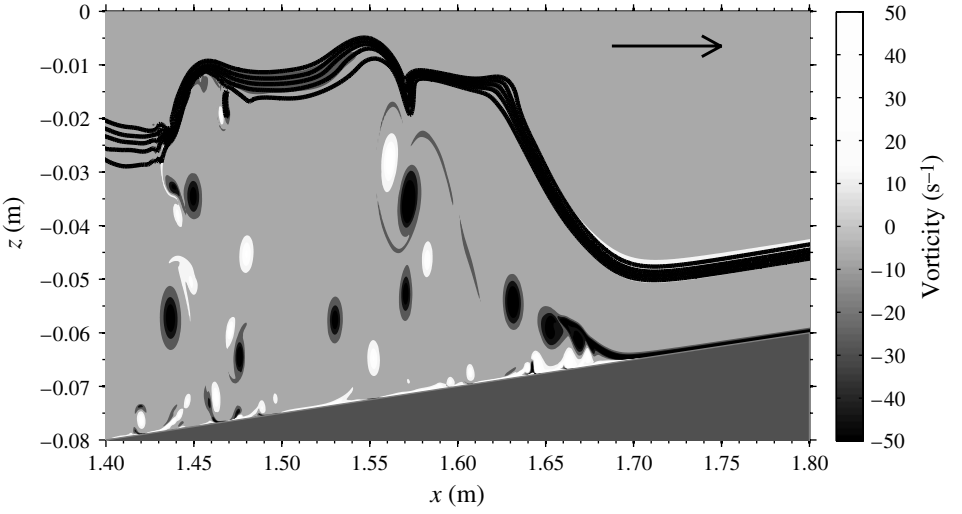


FIGURE 5. Same as figure 3, but for simulation 8A and corresponding to figure 4(*d*). The shed vortices beneath the rear face have lifted high enough to make the pycnocline unstable, leading to wave breaking.

to the separated flow and eddies when the first cluster of vortices are shed, with an average transfer rate of order 0.01% s^{-1}, and wave dynamics are not affected.

4.3. *Threshold of the vortex shedding*

To separate stable from unstable ISW boundary layers, we draw an analogy with aerodynamics research (e.g. Gaster 1969; Pauley *et al.* 1990), where bursting criteria for separation bubbles have been introduced in terms of the momentum-thickness Reynolds number at the separation point ($Re_{\theta_{sep}}$) and a dimensionless pressure gradient parameter ($\tilde{P} = \theta_{sep}^2/\nu \times \mathrm{d}U/\mathrm{d}x$).

To model the incipient threshold for vortex shedding, we consider the inviscid deceleration rate at the bottom ($\mathrm{d}U/\mathrm{d}x$ which can be obtained from solution of Euler equations), which controls the bubble shape (Gaster 1969; Pauley *et al.* 1990). In our viscous simulations $\mathrm{d}U/\mathrm{d}x$ may be computed from the free-stream velocity field above the bubble. Figure 6 shows the wave-induced horizontal velocity, horizontal velocity gradient and the pressure gradient distribution at the separation point (point of streamline detachment where $\partial u/\partial z = 0$) for simulation 6F for both viscous and inviscid cases (all measured at the same location in the inviscid simulation). The free-stream values are a reasonable measure of inviscid values when the bubble size is $\ll H$. This is particularly true for high-Reynolds-number simulations.

Following Gaster (1969) and Pauley *et al.* (1990) we plot their proposed pressure gradient parameters $\tilde{P} = \theta_{sep}^2/\nu \times (\mathrm{d}U/\mathrm{d}x)_{sep}$ and $\tilde{P}_{max} = \theta_{sep}^2/\nu \times (\mathrm{d}U/\mathrm{d}x)_{max}$ versus $Re_{\theta_{sep}}$ (figures 7*a* and 7*b*, respectively). Here $(\mathrm{d}U/\mathrm{d}x)_{max}$ is the maximum (negative) value of the inviscid horizontal velocity gradient along the bubble. Our results (figure 7*a*) do not agree with the instability criterion proposed by Gaster (1969). He employed an aerofoil, mounted above a flat plate, to produce an adverse pressure gradient on the surface of the plate; thus the separation was driven by the aerofoil geometry and his bursting criterion was only valid for his experimental setup. In the present study separation is induced by the curvature of the flow in the ISW

https://doi.org/10.1017/jfm.2011.432 Published online by Cambridge University Press

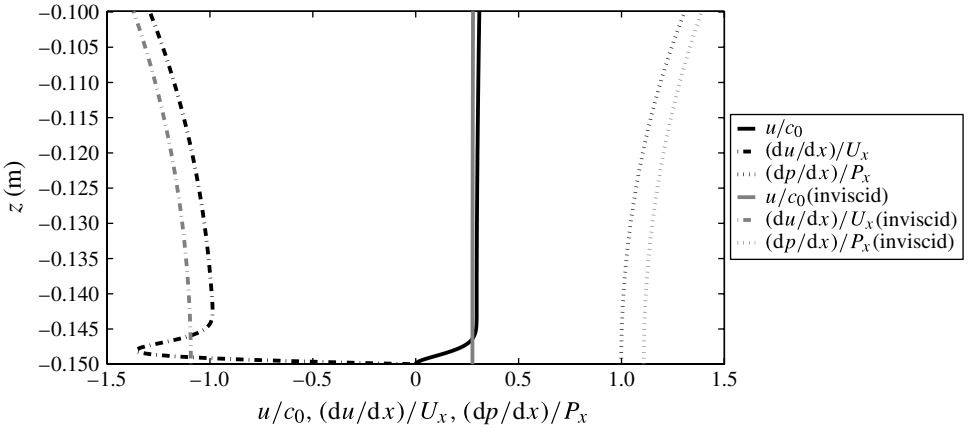


FIGURE 6. Non-dimensional horizontal velocity u/c_0 (solid line); horizontal velocity gradient scaled by the free-stream value at the edge of boundary layer, $((\mathrm{d}u/\mathrm{d}x)/U_x$; dash-dot line); and pressure gradient scaled by the free-stream value at the edge of boundary layer $((\mathrm{d}p/\mathrm{d}x)/P_x$; dotted line) at the separation point for simulation 6F. Inviscid values are in grey.

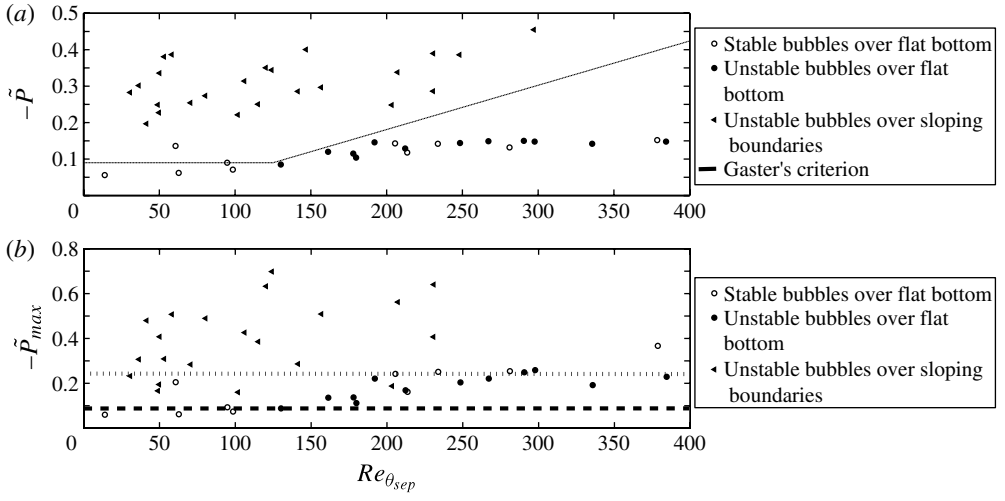


FIGURE 7. Bursting criteria proposed by (*a*) Gaster (1969) and (*b*) Pauley *et al.* (1990) as a function of the pressure gradient parameter and momentum-thickness Reynolds number. Horizontal dotted line represents the bursting criterion proposed by Pauley *et al.* (1990). All unstable cases in our simulations lie above the dashed line.

and has a much higher vertical to horizontal aspect ratio compared to aerodynamics studies. In comparison to Pauley *et al.* (1990), all of the unstable cases (leading to vortex shedding) lie above $-\tilde{P}_{max} \approx 0.09$ (figure 7*b*), smaller than their criterion $-\tilde{P}_{max} > 0.24$ and there are two stable bubbles modelled to be in the unstable region. These differences can be due to differences in the flow field driving the adverse pressure gradient. Pauley *et al.* (1990) used a local suction port on top of a horizontal channel to generate an adverse-pressure-gradient region.

https://doi.org/10.1017/jfm.2011.432 Published online by Cambridge University Press

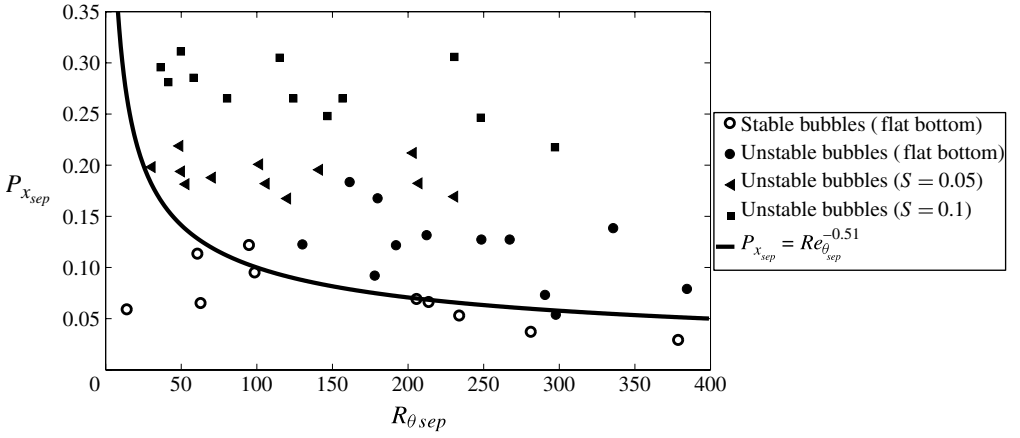


FIGURE 8. Stability criterion curve as a function of the non-dimensional free-stream pressure gradient ($P_{x_{sep}}$) and momentum thickness Reynolds number ($Re_{\theta_{sep}}$) at the toe of the separation bubble.

We find that stable and unstable separation bubbles can be categorized according to the free-stream pressure gradient, non-dimensionalized by $\rho_0 g'$ ($P_{x_{sep}} = (1/\rho_0 g')\,(\mathrm{d}P/\mathrm{d}x)_{sep}$), and $Re_{\theta_{sep}}$ (figure 8). The data shown are taken at the time when instability first occurred (instability waves; e.g. figure 2*b*) in the vorticity field. Here, we have incorporated our results over both flat and sloping bottom boundaries.

The onset of instability for a particular ISW occurs as follows. For an ISW travelling over a flat bottom, the pressure gradient external to the bubble is constant, and the bubble grows under its influence until steady state is reached (stable) or vortex shedding begins (unstable). If $(Re_{\theta_{sep}}, P_{x_{sep}})$ is above the threshold of instability curve (figure 8; $P_{x_{sep}} = Re_{\theta_{sep}}^{-.051}$, empirically defined based on our numerical results), the growing separation bubble becomes unstable to vortex shedding.

Over sloping bottom boundaries, the bubble grows within a continuously increasing adverse-pressure-gradient region until it becomes unstable to vortex shedding. All shoaling wave simulations lie above the stability curve (figure 8) because the rates of increase of $P_{x_{sep}}$ and $Re_{\theta_{sep}}$ are greater than the separation bubble growth rate. The bubble should grow sufficiently for the vortex shedding to start, indicating a time lag between variation in boundary layer characteristics (pressure gradient and momentum-thickness Reynolds number) relative to bubble growth. $P_{x_{sep}}$ and $Re_{\theta_{sep}}$ increase more rapidly over steeper slopes causing these data to lie above those for mild slopes.

A shoaling wave might experience polarity change (leading to fission), forward overturning (plunging) or surging while shed vortices reaching the pycnocline can lead to collapsing (Aghsaee *et al.* 2010). The latter case is shown in simulation 8A ($S = 0.05$), where shedding begins at $x = 1.35$ m (figure 4*b*) and breaking ultimately occurs at $x = 1.50$ m (figure 5). The distance between the shedding and breaking locations increases with decreasing boundary slope. Over steeper slopes the wave trough approaches the bottom boundary more rapidly, the rear face of the wave steepens faster and there is a greater rate of increase in the adverse pressure gradient. For very gentle slopes ($S \ll 0.05$), as are commonly found in oceanic flows, fission may occur, after vortex shedding. The wave slope and boundary slope parameter range over which this process will predominate has been identified (see Aghsaee *et al.* 2010, their figure 6). The boundary layer dynamics of the resulting waves of elevation has

https://doi.org/10.1017/jfm.2011.432 Published online by Cambridge University Press

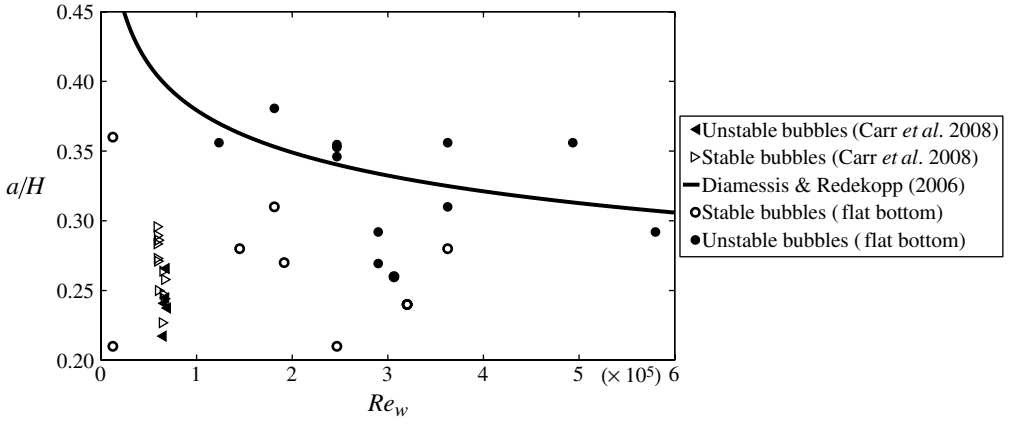


FIGURE 9. Stability diagram in non-dimensional wave amplitude (a/H) versus ISW Reynolds number ($Re_w = c_0 H/\nu$) space. The curved line represents the critical wave amplitude as $a_{cr} = 0.5\,(Re_w/10^4)^{-0.012}$ from Diamessis & Redekopp (2006). Laboratory data are from Carr *et al.* (2008).

been considered elsewhere (e.g. Stastna & Lamb 2008). Since the parameters $P_{x_{sep}}$ and $Re_{\theta_{sep}}$ cannot be feasibly measured in field experiments, we propose a more practical criterion to predict the occurrence of vortex shedding in § 5.

5. Discussion

5.1. *Vortex shedding criterion*

Generalizing our results to determine a criterion to predict vortex shedding beneath ISWs which can be readily computed from field data is a first step in determining where bottom boundary layer instability may occur in geophysical flows, potentially leading to localized sediment re-suspension. We find that the stability boundary for vortex shedding proposed by Diamessis & Redekopp (2006) – as discussed in § 1 – is inconsistent with our data, as it was with laboratory data of Carr *et al.* (2008) (figure 9). Overall, the results are mutually inconsistent: the unstable observations (leading to vortex shedding) from Carr *et al.* (2008) and 50 % of our unstable simulations lie in the stable region predicted by Diamessis & Redekopp's (2006) criterion. Besides the inappropriate choices of parameters they used for the pressure gradient and Reynolds number, some of these inconsistencies may result from Diamessis & Redekopp (2006) forcing KdV waves to have a/H as large as 0.3–0.6. Weakly nonlinear KdV theory cannot represent such large waves and models with higher-order of nonlinearity are required (Carr *et al.* 2008).

To generalize our results we estimate $Re_{\theta_{sep}} = U\theta_{sep}/\nu$ and $P_{x_{sep}} = (1/\rho_0 g')\,(\mathrm{d}P/\mathrm{d}x)_{sep}$ in terms of parameters that are more readily measured in the field. From (2.5), we find $(U + c)\,(\mathrm{d}U/\mathrm{d}x)_{sep} \approx -(1/\rho_0)\,(\mathrm{d}P/\mathrm{d}x)_{sep}$ where U and $\mathrm{d}U/\mathrm{d}x$ are free-stream values above the boundary layer at the separation point (figure 10). $U + c$ represents the fluid velocity in a frame of reference moving with wave speed c, in which the flow evolves on a slow time scale before instability occurs. The phase speed associated with a shoaling wave is not constant, due to the change in water depth. The phase speed was approximated, at the bubble location, to equal the progressive speed of the bubble core at the initiation of boundary layer instability. Owing to uncertainties

https://doi.org/10.1017/jfm.2011.432 Published online by Cambridge University Press

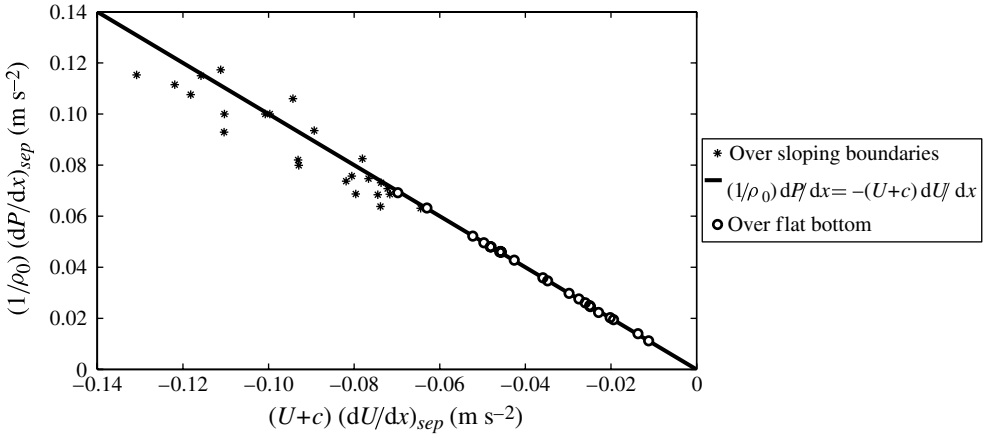


FIGURE 10. Free-stream pressure gradient, $(1/\rho_0)\,\mathrm{d}P/\mathrm{d}x$ versus $(U+c)\,\mathrm{d}U/\mathrm{d}x$ at the separation point.

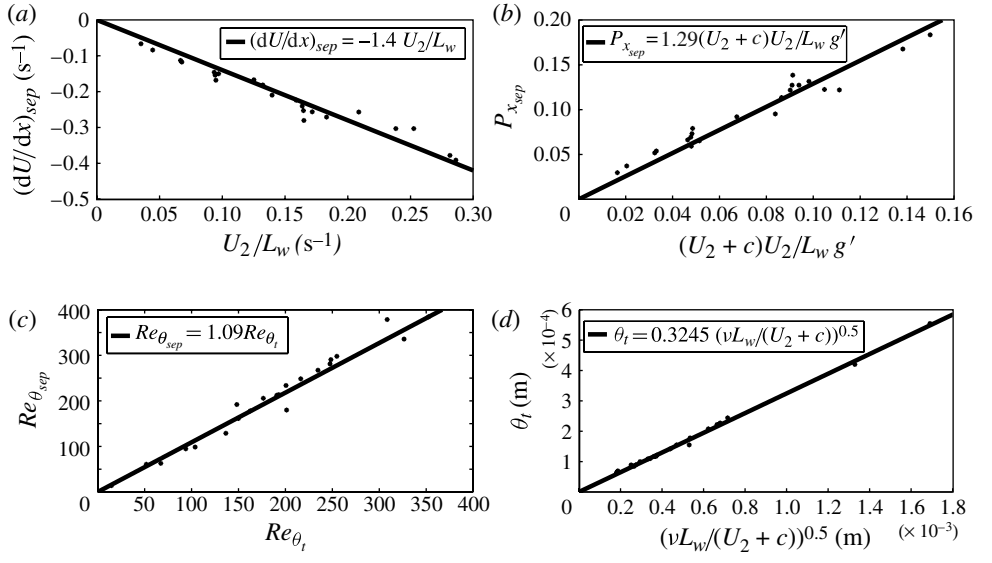


FIGURE 11. (*a*) Free-stream horizontal velocity gradient, $\mathrm{d}U/\mathrm{d}x$ at the separation point versus ratio of free-stream lower-layer horizontal velocity at the wave trough to horizontal wavelength, U_2/L_w. (*b*) Free-stream non-dimensional pressure gradient, $P_{x_{sep}}$ at the separation point versus $(U+c)U_2/L_w g'$. (*c*) Momentum-thickness Reynolds number at the separation point, $Re_{\theta_{sep}}$ as a function of the momentum-thickness Reynolds number beneath the wave trough Re_{θ_t}. (*d*) Momentum thickness beneath the wave trough θ_t as a function of $\sqrt{\nu L_w/(U_2+c)}$.

in the relation between this estimate and the actual phase speed, scatter in the data over sloping boundaries is not surprising (figure 10).

The horizontal velocity varies from its maximum at the wave trough to zero at the wave shoulder (figure 1) and so $U_2/L_w \approx -\mathrm{d}U/\mathrm{d}x$ at the separation point (figure 11*a*), where U_2 is the free-stream horizontal velocity beneath the wave trough. The

https://doi.org/10.1017/jfm.2011.432 Published online by Cambridge University Press

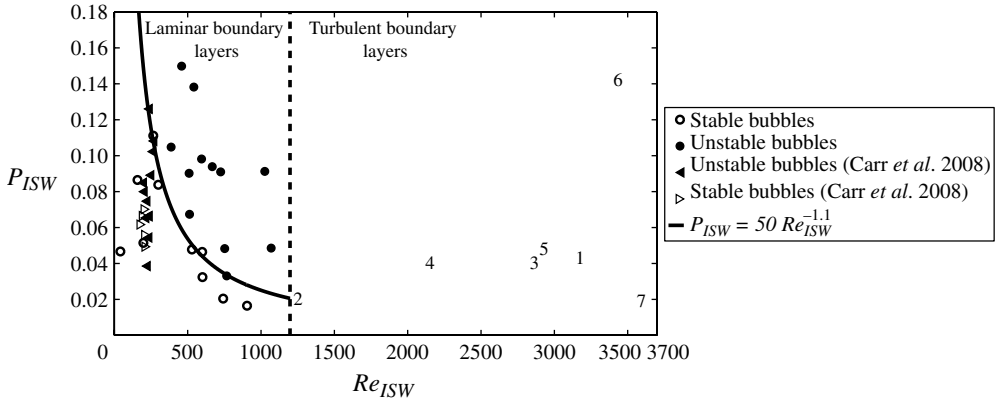


FIGURE 12. Stability criterion curve parameterized as a function of P_{ISW} and Re_{ISW} with laboratory data from Carr *et al.* (2008) and published field data represented by numbers 1 to 7 (see table 3).

non-dimensionalized pressure gradient at the separation point correlates with

$$P_{x_{sep}} \approx P_{ISW} = (U_2 + c)\frac{U_2}{L_w g'} \tag{5.1}$$

(figure 11*b*), which is more readily measured in the field.

Looking for an estimation for $Re_{\theta_{sep}}$ we realize that it correlates with the momentum-thickness Reynolds number under the wave trough ($Re_{\theta_t} = U_2\theta_t/\nu$; figure 11*c*) where θ_t is the momentum thickness under the wave trough. Thus we only need to parameterize θ_t, where we follow Schlichting (1979) and balance friction with inertia in a steady-state flow. This gives $U_2/\theta_t^2 \sim \rho(U_2 + c)U_2/L_w$ leading to $\theta_t \approx \sqrt{\nu L_w/(c + U_2)}$ as a measure of boundary layer thickness beneath the ISW trough (figure 11*d*) and

$$Re_{\theta_{sep}} \approx Re_{\theta_t} \approx Re_{ISW} = U_2\sqrt{\frac{L_w}{\nu(U_2 + c)}} \tag{5.2}$$

can be used as a measure of the boundary-layer Reynolds number. Combining our data and the Carr *et al.* (2008) laboratory data in P_{ISW} versus Re_{ISW} space (figure 12), we find a suitable parameterization for vortex shedding over flat bottom boundaries. Since the wave parameters (wave amplitude, wavelength and velocity field) change as an ISW shoals, it is not possible to predict where shedding starts over sloping boundaries.

Carr *et al.* (2008) did not report the horizontal velocity at the wave trough, U_2, which we calculated using (2.6). L_w was obtained from (2.4), where the volume of fluid displaced by the wave was taken to be equal to the fluid volume released from behind the gate-type wavemaker (M. Carr, personal communication). Nearly all of the released fluid forms a single ISW of depression (Michallet & Ivey 1999; Carr *et al.* 2008) thus $L_w = V_{step}/Ba$ where V_{step} is the volume of upper-layer fluid released from behind the gate and B is the tank width.

A best-fit power law to the data yields a vortex shedding criterion of

$$P_{ISW} = \frac{50}{Re_{ISW}^{1.1}} \tag{5.3}$$

https://doi.org/10.1017/jfm.2011.432 Published online by Cambridge University Press

Wave	c (m s^{-1})	U_2 (m s^{-1})	L_w (m)	Re_{ISW}	P_{ISW}
1: Vlasenko, Brandt & Rubino (2000), North of the strait of Messina	1.00	0.20	300	3162	0.042
2: Vlasenko *et al.* (2000), South of the strait of Messina	1.20	0.10	200	1240	0.019
3: Bourgault & Kelley (2003), St. Lawrence River	0.70	0.25	124	2845	0.040
4: Moum *et al.* (2003), Oregon Shelf	0.60	0.15	150	2147	0.040
5: Orr & Mignerey (2003), South China Sea wave B	0.99	0.25	170	2901	0.047
6: Quaresma *et al.* (2007), Portuguese shelf	0.34	0.25	110	3414	0.140
7: Shroyer *et al.* (2009), wave Tonya, New Jersey Coast	0.73	0.25	200	3571	0.018

TABLE 3. Parameters calculated from published field observations used to test the criterion shown in figure 12.

(figure 12). This encompasses all of our unstable simulations as well as ∼18 % of the unstable experiments from Carr *et al.* (2008). Possible reasons for the discrepancy between our results and those of Carr *et al.* (2008) are: (*a*) the laboratory observed instabilities are primarily three-dimensional; (*b*) errors in the estimation of U_2 and L_w; (*c*) the lack of finite-amplitude perturbations in the numerical solution from which instabilities will grow through the phenomenon of subcritical transition (Stefanakis 2010); and (*d*) existence of an oscillatory background barotropic flow in lab experiments, generated during the gate release, which may have influenced vortex generation (M. Carr, personal communication).

Our two-dimensional domain limits the extension of (5.3) to higher Reynolds numbers where the flow may be expected to become three-dimensional and turbulent. For his aerofoil-plate apparatus, Gaster (1969) mentioned that the boundary layer will be laminar if the displacement-thickness Reynolds number (where displacement thickness is $\delta^* = \int_0^{z(U)} (1 - u/U)\,\mathrm{d}z$) is less than ∼1000. Applying this limit to our data suggests that the boundary layer beneath ISWs is laminar when $Re_{ISW} <\sim 1200$. A turbulent boundary layer will require a stronger pressure gradient to undergo flow separation and possible global instability (see § 2), potentially shifting the curve (5.3) to higher values. However, the leading edge of the ISW has a favourable pressure gradient, which can suppress ambient turbulence and re-laminarize the boundary layer upstream of the separation point (e.g. Bourassa & Thomas 2009). For these reasons we do not extend (5.3) beyond $Re_{ISW} >\sim 1200$ (figure 12). Field data and high-Reynolds-number three-dimensional simulations are needed to investigate stability in this regime.

To apply the proposed parameterization to field conditions, requires *in-situ* observations of the horizontal current structure beneath the wave trough, the ISW wavelength and the ISW phase speed. These parameters can be computed from typical deployed instruments, including an acoustic Doppler current profiler (for the velocity field) and thermistor chains (for the wavelength and phase speed). We computed P_{ISW} and Re_{ISW} from published field observations (table 3 and figure 12) and all waves lie in the turbulent region.

The stability characteristics of the observed waves were not reported. Of the waves shown, only Quaresma *et al.* (2007), figure 15 therein, reported concurrent sediment

https://doi.org/10.1017/jfm.2011.432 Published online by Cambridge University Press

suspension observations, beneath ISWs of depression (table 3; wave 6 representing their leading wave). Although that wave lies in the turbulent region, it has induced a strong pressure gradient suggesting that global instability is leading to re-suspension (figure 12). The stability characteristics of these waves will also be influenced by bottom roughness and background flow, which have not been investigated herein (e.g. Stastna & Lamb 2008; Carr, Stastna & Davies 2010).

5.2. *Application to three-dimensional flows*

To apply the low-Reynolds-number two-dimensional results presented herein to field observations requires consideration of Reynolds number effects, including potential three-dimensionality of the flow as Reynolds number increases. We first consider three-dimensional effects at low Reynolds number. From direct numerical simulations of flow separation on an aerofoil, Jones *et al.* (2008) found that the initial vortex shedding phenomenon retains its predominantly two-dimensional structure, with three-dimensional secondary perturbations appearing after the first cluster of eddies have been shed. Similarly, laboratory observations of flow separation beneath shoaling ISWs (Boegman & Ivey 2009) also show the initial stages of instability to be two-dimensional , with coherent spanwise vortex tubes across the flume width.

Direct comparisons between the laboratory results and the shoaling ISW simulations presented herein (Lamb, Boegman & Ivey 2005) show the initial stages of wave breaking to be well simulated, including the formation of two boluses (figure 13*b*,*c*), which occur as a result of instability of the separated boundary layer flow beneath the shoaling wave (see Aghsaee *et al.* 2010). The inability of the two-dimensional model to capture lateral three-dimensional secondary instability is clear during the latter stages of wave breaking, (figure 13*d*), where the plunging wave crest and vortex structures persist in the two-dimensional simulations. Global instability and sediment re-suspension (Boegman & Ivey 2009) occur prior to these secondary three-dimensional effects.

5.3. *Implications for sediment re-suspension*

To assess the potential for ISW-induced sediment re-suspension, we examine the simulated shear stress fields during boundary layer instability. The contribution of bed shear stress to sediment re-suspension is typically assessed using the Shields parameter (e.g. Drake & Cacchione 1986; Quaresma *et al.* 2007). For a given grain size, if the Shields parameter reaches a threshold value, the bed shear stress is capable of incipient sediment motion leading to bed-load transport, but not necessarily sediment re-suspension. We observe the instantaneous bed shear stress increasing by a factor of 2.4 on the flat bottom after global instability occurs and the first vortices are shed (figure 14*a*; simulation 12F), close to the factor of 2.7 observed by Stastna & Lamb (2002) under ISWs of elevation; while an increase up to a factor of 5 was reported by Diamessis & Redekopp (2006) under their KdV waves. Over sloping topography (figure 14*b*; simulation 1A) the shear stress increases by a factor of 7 due to global instability.

Boegman & Ivey (2009) argued that elevated near-bottom vertical velocities are also required to suspend the motile sediments in the water column. We observed elevated vertical velocities associated with vortex shedding, which over flat bottoms can ascend to 10 % of the total depth from the bed in the initial two-dimensional shedding stage (figure 15). This value can increase up to a maximum of 33 % at later stages (simulation 12F), and in simulations of Stastna & Lamb (2008) was close to 25 %. These are greater than the 17 % achieved in the laboratory (Carr *et al.* 2008), where

https://doi.org/10.1017/jfm.2011.432 Published online by Cambridge University Press

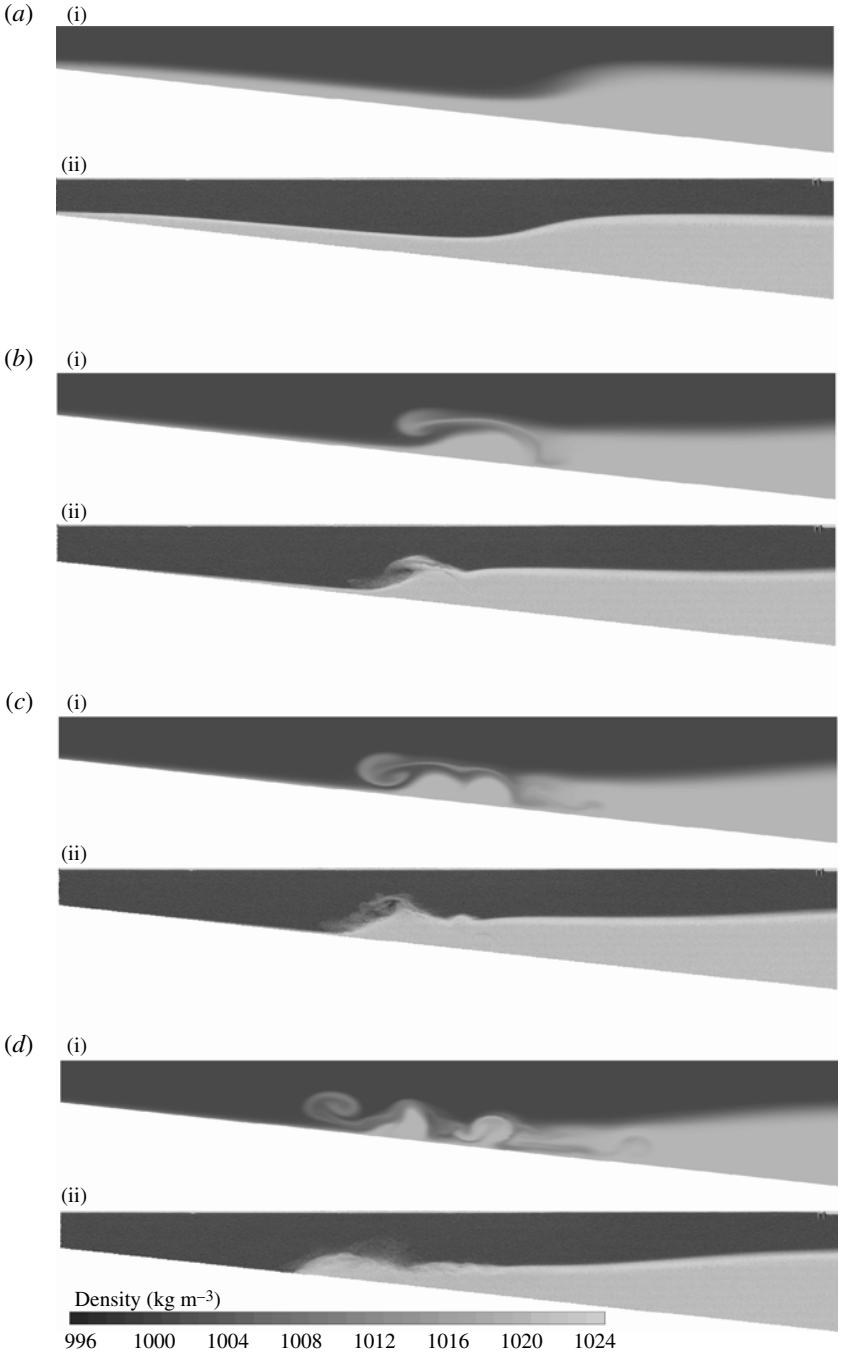


FIGURE 13. Comparison of two-dimensional model results to experimental observations of shoaling ISWs from Boegman *et al.* (2005) where in each pair of figures, panels (i) and (ii) represent density field associated with numerical simulation and lab experiment respectively. time increases from (*a*) to (*d*). Further details of the simulations and experimental comparison can be found in Lamb *et al.* (2005).

https://doi.org/10.1017/jfm.2011.432 Published online by Cambridge University Press

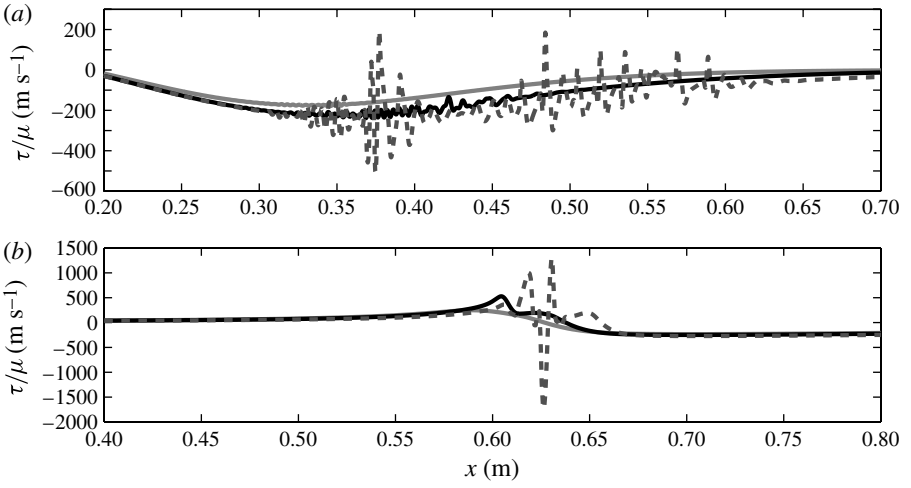


FIGURE 14. Temporal increase of instantaneous bed shear stress (scaled by $\mu_2 = \nu\rho_2 = 5.2 \times 10^{-5}$ kg m^{-1} s^{-1}) due to vortex shedding: (*a*) simulation 12F over a flat bottom. Solid grey line and solid black line correspond to $t^* = tc_0/H = 1.42, 2.19$, respectively, and dashed grey line corresponds to $t^* = 2.95$, when the first vortices have been shed. (*b*) Simulation 1A over a sloping bottom. Solid grey line and solid black line correspond to $t^* = tc_0/H = 12.38, 12.66$ respectively and dashed grey line correspond to $t^* = 13.07$, when the first vortices have been shed.

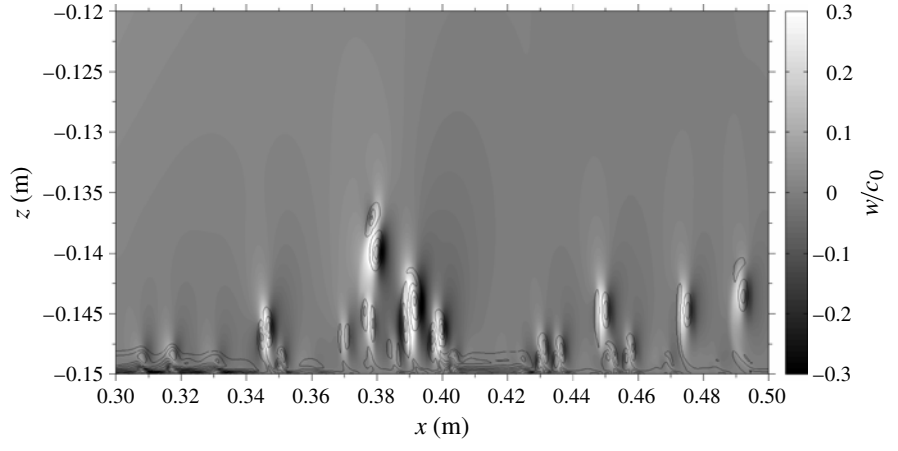


FIGURE 15. Instantaneous non-dimensional vertical velocity w/c_0 (shaded) and vorticity field contours (black contours) for simulation 5F at $t^* = tc_0/H = 2.42$. Elevated vertical velocities are due to vortex shedding.

secondary three-dimensional effects are likely to lead to more rapid degeneration of the shed vortices as they ascend through the water column (e.g. figure 13). ISW-induced re-suspension has been observed, in the coastal ocean, to ascend as high as 50 % of an 80 m water column (Quaresma *et al.* 2007).

The maximum vertical velocities associated with the shed eddies, over a flat bottom, at the initiation of the two-dimensional instability are $0.1 < w_{max}/c_0 < 0.7$ (table 1),

https://doi.org/10.1017/jfm.2011.432 Published online by Cambridge University Press

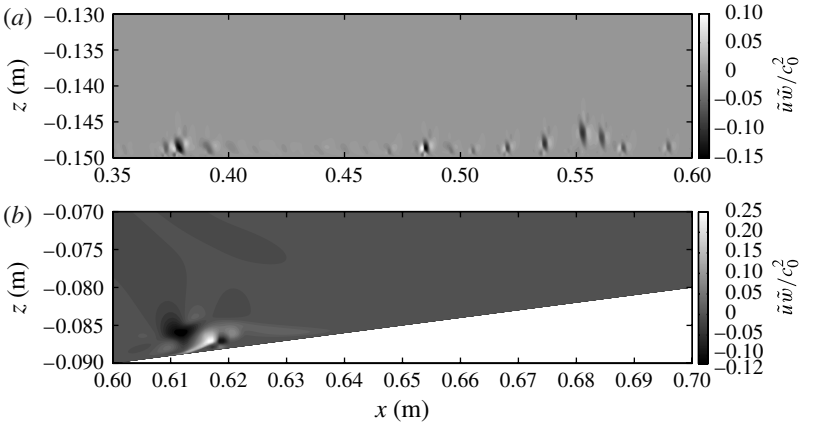


FIGURE 16. Non-dimensionalized Reynolds stress $\tilde{u}\tilde{w}/c_0^2$: (*a*) simulation 12F at $t^* = tc_0/H = 2.95$ with maximum $\tilde{u}\tilde{w}/c_0^2 = 0.1 > 0.05$ and (*b*) simulation 1A at $t^* = tc_0/H = 12.8$ with a maximum of $\tilde{u}\tilde{w}/c_0^2 = 0.25 > 0.05$, both indicating locations of potential bed sediment re-suspension.

consistent with Diamessis & Redekopp (2006) who found $w_{max} \to c_0$. Carr *et al.* (2008) observed a narrower range of much smaller maximum vertical velocities $0.02 < w_{max}/c_0 < 0.06$. These differences between simulations and experiments are likely to be Reynolds number effects; w_{max}/c_0 scales with the momentum-thickness Reynolds number and adverse pressure gradient (tables 1 and 2). If three-dimensional effects are neglected, Carr *et al.* (2008) most probably observed weak vortex shedding leading to small vertical velocities because they covered a narrow range of relatively small Reynolds numbers (figure 12).

For shoaling waves, the larger the vertical velocities ($w_{max} \to 1.81c_0$), higher bed shear and greater energy transfer to the separation bubble (discussed at § 4), compared to flat bottom simulations, suggests the important role of shoaling ISWs in bed sediment re-suspension along sloping regions of lakes and oceans. Boegman & Ivey (2009) directly correlated the near-bed non-dimensional Reynolds stress $\tau_R = \tilde{u}\tilde{w}/c_0^2$ to re-suspension during instability of shoaling waves, where $(\tilde{u}, \tilde{w})$ are the vortex-coherent fluctuating horizontal and vertical velocity fields resulting from the induced near-bed vortices, respectively, relative to the mean flow. This value is smaller than the maximum simulated values of 0.10 and 0.25 over flat (12F, figure 16*a*) and sloping (1A $S = 0.1$, figure 16*b*) bottoms, respectively, indicating that the two-dimensional model captures realistic near-bed stresses capable of re-suspension.

6. Conclusions

We have investigated laminar boundary layer instability and subsequent vortex shedding beneath ISWs over both flat and sloping bottoms. A threshold for vortex shedding was found to be dependent on a non-dimensional pressure gradient and the momentum-thickness Reynolds number at the separation point. Over flat bottoms, vortex shedding was more probable beneath broad-crested ISWs, which have steeper wave slopes, greater lower-layer velocities and consequently stronger adverse pressure gradients, relative to narrow-crested ISWs which have smaller amplitudes. Vortex shedding always occurs beneath shoaling ISWs owing to the continuously increasing adverse pressure gradient associated with nonlinear steepening and strengthening

https://doi.org/10.1017/jfm.2011.432 Published online by Cambridge University Press

near-bottom currents as the waves shoal. We have shown that the non-dimensionalized wave amplitude and total-depth Reynolds number are not suitable for separating waves with stable and unstable boundary layers. Combining our results with published laboratory data, we proposed a vortex shedding criterion, which is a function of the boundary-layer Reynolds number and non-dimensional pressure gradient parameter (5.3) associated with an ISW. These parameters can be readily measured in field experiments.

The simulated vertical velocities and near-bed Reynolds stresses were found to be sufficient to re-suspend bed sediments, in comparison to published laboratory results. However, both our results and prior works fail to consider the effects of large Reynolds number and the presence of a pre-existing turbulent bottom boundary layer on the adverse-pressure-gradient-driven dynamics and re-suspension. This requires further investigation and may be conducted using large-scale three-dimensional simulations (e.g. Barad & Fringer 2010) and/or laboratory experiments. Future work should also consider bottom roughness and sediment grain size. Field experiments are ultimately required to validate and test the fidelity of the results presented herein.

Acknowledgements

The authors thank Magda Carr for discussions and providing laboratory data. The research was funded by NSERC Discovery grants to L.B. and K.G.L. and by Queen's University. P.J.D. acknowledges support from ONR Physical Oceanography grant N00014-07-1-0957 and NSF-OCE CAREER Award No. 0845558.

REFERENCES

AGHSAEE, P., BOEGMAN, L. & LAMB, K. G. 2010 Breaking of shoaling internal solitary waves. *J. Fluid Mech.* **659**, 289–317.

APEL, J. R. 2002 Oceanic internal waves and solitons. In *An Atlas of Oceanic Internal Solitary Waves*. Global Ocean Associates.

BARAD, M. F. & FRINGER, O. B. 2010 Simulations of shear instabilities in interfacial gravity waves. *J. Fluid Mech.* **644**, 61–95.

BOEGMAN, L., IMBERGER, J., IVEY, G. N. & ANTENUCCI, J. P. 2003 High-frequency internal waves in large stratified lakes. *Limnol. Oceanogr.* **48**, 895–919.

BOEGMAN, L. & IVEY, G. N. 2009 Flow separation and resuspension beneath shoaling nonlinear internal waves. *J. Geophys. Res.* **114**, C02018.

BOGUCKI, D. J., DICKEY, T. & REDEKOPP, L. G. 1997 Sediment resuspension and mixing by resonantly generated internal solitary waves. *J. Phys. Oceanogr.* **27**, 1181–1196.

BOGUCKI, D. J. & REDEKOPP, L. G. 1999 Global instability of separated flows: a paradigm for sediment resuspension by internal waves. *Geophys. Res. Lett.* **26**, 1317–1320.

BOGUCKI, D. J., REDEKOPP, L. G. & BARTH, J. 2005 Internal solitary waves in the coastal mixing and optics 1996 experiment: multimodal structure and re-suspension. *J. Geophys. Res.* **110**, C02024.

BONNIN, J., VAN HAREN, H., HOSEGOOD, PH. & BRUMMER, G. A. 2006 Burst resuspension of seabed material at the foot of the continental slope in the Rockall Channel. *Mar. Geol.* **226**, 167–184.

BOURASSA, C. & THOMAS, F. O. 2009 An experimental investigation of a highly accelerated turbulent boundary layer. *J. Fluid Mech.* **634**, 359–404.

BOURGAULT, D. & KELLEY, D. E. 2003 Wave-induced mixing in a partially mixed estuary. *J. Mar. Res.* **226**, 553–576.

https://doi.org/10.1017/jfm.2011.432 Published online by Cambridge University Press

BUTMAN, B., ALEXANDER, P. S., SCOTTI, A., BEARDSLEY, R. C. & ANDERSON, S. P. 2006 Large internal waves in Massachusetts Bay transport sediments offshore. *Cont. Shelf Res.* **26**, 2029–2049.

CARR, M. & DAVIES, P. A. 2006 The motion of an internal solitary wave of depression over a fixed bottom boundary in a shallow, two layer fluid. *Phys. Fluids* **18**, 016601.

CARR, M., DAVIES, P. A. & SHIVARAM, P. 2008 Experimental evidence of internal solitary wave-induced global instability in shallow water benthic boundary layers. *Phys. Fluids* **20**, 066603.

CARR, M., STASTNA, M. & DAVIES, P. A. 2010 Internal solitary wave-induced flow over a corrugated bed. *Ocean Dyn.* **60**, 1007–1025.

DIAMESSIS, P. & REDEKOPP, L. G. 2006 Numerical investigation of solitary internal wave-induced global instability in shallow water benthic boundary layers. *J. Phys. Oceanogr.* **36**, 784–812.

DRAKE, D. E. & CACCHIONE, D. A. 1986 Field observations of bed shear stress and sediment resuspension on continental shelves, Alaska and California. *Cont. Shelf Res.* **6, 3**, 415–429.

GASTER, M. 1969 The structure and behaviour of laminar separation bubbles. *AGARD CP* **4**, 813–854.

HELFRICH, K. R. & MELVILLE, W. K. 1986 On long nonlinear internal waves over slope-shelf topography. *J. Fluid Mech.* **167**, 285–308.

HELFRICH, K. R. & MELVILLE, W. K. 2006 Long nonlinear internal waves. *Annu. Rev. Fluid Mech.* **38**, 395–425.

HOLLOWAY, P. E. 1987 Internal hydraulic jumps and solitons at a shelf break region on the Australian North West Shelf. *J. Geophys. Res.* **92**, 5405–5416.

HOSEGOOD, H. & VAN HAREN, 2004 Near-bed Solibores over the continental slope in the Faeroe–Shetland Channel. *Deep-Sea Res.* II **51**, 2943–2971.

HUERRE, P. 2000 Open shear flow instabilities. In *Perspectives in Fluid Dynamics* (ed. G. K. Batchelor, H. K. Moffatt & M. G. Worster), pp. 159–229. Cambridge University Press.

JACKSON, C. 2007 Internal wave detection using the Moderate Resolution Imaging Spectroradiometer. *J. Geophys. Res.* **112**, C11012.

JONES, L. E., SANDBERG, R. D. & SANDHAM, N. D. 2008 Direct numerical simulations of forced and unforced separation bubbles on an aerofoil at incidence. *J. Fluid Mech.* **602**, 175–207.

KLYMAK, J. M. & MOUM, J. N. 2003 Internal solitary waves of elevation advancing on a shoaling shelf. *Geophys. Res. Lett.* **30** (20), 2045.

KOOP, C. G. & BUTLER, G. 1981 An investigation of internal solitary waves in a two-fluid system. *J. Fluid Mech.* **112**, 225–251.

LAMB, K. G. 2002 A numerical investigation of solitary internal waves with trapped cores formed via shoaling. *J. Fluid Mech.* **451**, 109–144.

LAMB, K. G., BOEGMAN, L. & IVEY, G. N. 2005 Numerical simulations of shoaling internal solitary waves in tilting tank experiments. In *Proc. 9th European Workshop on Physical Processes in Natural Waters. Lancaster University*, pp. 31–38.

LAMB, K. G. & NGUYEN, V. T. 2009 Calculating energy flux in internal solitary waves with an application to reflectance. *J. Phys. Oceanogr.* **39**, 559–580.

LAMB, K. G. & WAN, B. 1998 Conjugate flows and flat solitary waves for a continuously stratified fluid. *Phys. Fluids* **10**, 2061–2079.

LEMCKERT, C., ANTENUCCI, J., SAGGIO, A. & IMBERGER, J 2004 Physical properties of turbulent benthic boundary layers generated by internal waves. *J. Hydraul. Engng ASCE* **130**, 58–69.

LIU, A. K., CHANG, Y. S., HSU, M.-K. & LIANG, N. K. 1998 Evolution of nonlinear internal waves in the East and South China seas: advances in Oceanography and Sea Ice Research: using ERS observations. *J. Geophys. Res.* **103**, 7995–8008.

MICHALLET, H. & IVEY, G. N. 1999 Experiments on mixing due to internal solitary waves breaking on uniform slopes. *J. Geophys. Res.* **104**, 13467–13477.

MOUM, J. N., FARMER, D. M., SMYTH, W. D., ARMI, L. & VAGLE, S. 2003 Structure and generation of turbulence at interfaces strained by internal solitary waves propagating shoreward over the continental shelf. *J. Phys. Oceanogr.* **33**, 2093–2112.

NIMMO SMITH, W. A. M., KATZ, J. & OSBORN, T. R. 2005 On the structure of turbulence in the bottom boundary layer of the coastal ocean. *J. Phys. Oceanogr.* **35**, 72–93.

https://doi.org/10.1017/jfm.2011.432 Published online by Cambridge University Press

ORR, M. H. & MIGNEREY, P. C. 2003 Nonlinear internal waves in the South China Sea: observation of the conversion of depression internal waves to elevation internal waves. *J. Geophys. Res.* **108** (C3), 3064.

OSTROVSKY, L. A. & STEPANYANTS, Y. A. 2005 Internal solitons in laboratory experiments: comparison with theoretical models. *Chaos* **15**, 037111:1–037111:28.

PAULEY, L. L., MOIN, P. & REYNOLDS, W. C. 1990 The structure of two-dimensional separation. *J. Fluid Mech.* **220**, 397–411.

QUARESMA, L. S., VITORINO, J., OLIVEIRA, A. & DA SILVA, J. 2007 Evidence of sediment resuspension by nonlinear internal waves on the western Portuguese mid-shelf. *Mar. Geol.* **246**, 123–143.

REEDER, D. B., MA, B. B. & YANG, Y. J. 2011 Very large subaqueous sand dunes on the upper continental slope in the South China Sea generated by episodic, shoaling deep-water internal solitary waves. *Mar. Geol.* **279**, 12–18.

SCHLICHTING, H. 1979 *Boundary-layer Theory*, 7th edn. McGraw-Hill.

SHROYER, E. L., MOUM, J. N. & NASH, J. D. 2009 Observations of polarity reversal in shoaling nonlinear internal waves. *J. Phys. Oceanogr.* **39**, 691–701.

STASTNA, M. & LAMB, K. G. 2002 Vortex shedding and sediment resuspension associated with the interaction of an internal solitary wave and the bottom boundary layer. *Geophys. Res. Lett.* **29** (0) doi:10.1029/2001GL014070.

STASTNA, M. & LAMB, K. G. 2008 Sediment resuspension mechanisms associated with internal waves in coastal waters. *J. Geophys. Res.* **113**, C10016.

STEFANAKIS, THEMISTOKLIS 2010 Bottom boundary layer instabilities induced by nonlinear internal waves. MSc thesis. School of Civil and Environmental Engineering, Cornell University.

SVEEN, J. K., GUO, Y., DAVIES, P. A. & GRUE, J. 2002 On the breaking of internal solitary waves at a ridge. *J. Fluid Mech.* **469**, 161–188.

VLASENKO, V., BRANDT, P. & RUBINO, A. 2000 Structure of large-amplitude internal solitary waves. *J. Phys. Oceanogr.* **30**, 2172–2185.

WANG, B. J., BOGUCKI, D. J. & REDEKOPP, L. G. 2001 Internal solitary waves in a structured thermocline with implications for resuspension and the formation of thin particle-laden layers. *J. Geophys. Res.* **106**, 9565–9585.

WARN-VARNAS, A. C., CHIN-BING, S. A., KING, D. B., HAWKINS, J. A., LAMB, K. G. & LYNCH, J. F. 2007 Winter PRIMER ocean-acoustic solitary wave modelling studies. *IEEE J. Ocean. Engng* **32**, 436–452.

https://doi.org/10.1017/jfm.2011.432 Published online by Cambridge University Press